

Analytical view factor solutions of a spherical cap from an infinitesimal surface

Kaname Sasaki*, Maciej Sznajder

DLR German Aerospace Center, Institute of Space Systems, Robert-Hooke-Str. 7, 28359 Bremen, Germany

Abstract

Under the assumption of diffuse surfaces, the amount of radiative heat transfer between two surfaces can be evaluated by a view factor. In the past, analytical view factor solutions were derived for many types of geometries. However, view factor solutions of a spherical cap, which is a part of a sphere cut off by a plane, from an infinitesimal surface have not been thoroughly investigated. In this study, geometrical configurations of a spherical cap and an infinitesimal surface are classified into different cases, and an analytical solution is derived for each case. Actual view factor values are calculated for various configurations, and the results are verified by view factors acquired by the numerical methods.

Keywords: View factor, Spherical cap, Radiative heat transfer

1. Introduction

In many engineering applications, it is common to evaluate radiative heat transfer between surfaces based on the assumption of diffuse radiation and reflections. In such cases, the amount of radiative energy emitted from one surface and reaching to another surface is determined by a view factor, which describes the geometrical relation of the two surfaces. In the past researches, analytical view factor solutions were derived for many types of geometries, and the collection of available view factors was compiled by Howell [1, 2].

With regard to a sphere and a circular disk related view factors, numbers of studies have been performed for different geometrical configurations. Cunningham derived view factors of a sphere from an arbitrary oriented infinitesimal surface [3]. Chung and Naraghi performed extensive investigation on view factors of a sphere [4], and variety of axisymmetric geometries [5, 6]. Also the view factor of a circular disk from an infinitesimal surface was studied by Naraghi [7], and Cabeza-Lainez [8, 9]. View factors from an infinitesimal surface to a spherical or a circular surface have practical applications in different engineering fields. Various studies can be found regarding the radiative heat exchange between an Earth orbiting satellite and the Earth [3, 10–20], the evaluation of thermal radiation from a fireball caused by hazardous material [21–25], and the evaluation of lighting conditions in the field of architecture [26].

In this article, new analytical view factor solutions of a spherical cap, which is a part of a sphere cut off by a plane, are presented. Compared to the sphere view factor, the spherical cap view factor extends the application possibility in terms of geometry, and it also enables users to evaluate spherical shape section-wise. That means that the variable temperature or variable thermal properties on the surface can be considered in the analytical evaluation. In the entire discussion, a view factor of a spherical cap means a view factor from an infinitesimal surface towards the convex side of the spherical cap surface. View factors of the same type of geometry was studied by Naraghi [27]. However, the reported solutions were limited to some specific configurations. The solutions acquired in this study cover arbitrary size and relative positions of a spherical cap and an infinitesimal surface. In addition, the classification process to determine a solution for an arbitrary configuration is presented.

*Corresponding author.

Email address: kaname.sasaki@dlr.de (Kaname Sasaki*)

Nomenclature

α	angular parameter for the L_2 integration	ψ	angle between the captop direction and the direction to the cap edge
α_1	α value for the intersection of the spherical cap edge and the projection plane edge	θ	angle between the Z axis and a tangential line from the infinitesimal surface to the sphere
α_2, α_3	α values for the intersections of the spherical cap edge and the view edge	θ'	transformed θ for Case 18 and 19 configurations
α_{end}	ending angle of the L_2 integration	Θ_0	angle between the normal vector of the infinitesimal surface and the line to a spherical surface facet
α_{start}	starting angle of the L_2 integration	Θ_1	angle between the normal vector of a spherical surface facet and the line to the infinitesimal surface
β	angular parameter for the L_1 integration	φ	angle between the captop direction and the $-Z$ direction from the sphere center
β_0	β value for the intersection of the view edge and the projection plane edge	d	distance between the spherical cap center and the infinitesimal surface
β_1	β value for the intersection of the spherical cap edge and the projection plane edge	d'	transformed d for Case 18 and 19 configurations
β_2, β_3	β values for the intersections of the spherical cap edge and the view edge	F_i	view factor of Case i ($i = 1, 2, \dots, 21$)
β_{end}	ending angle of the L_1 integration	h	distance from the infinitesimal surface to the projection plane
β_{start}	starting angle of the L_1 integration	L_i	line integration of type i ($i = 1, 2, 3, 4$)
$\mathbf{x}_2, \mathbf{x}_3$	intersections of the spherical cap edge and the view edge	R	radius of the projection plane
\mathbf{x}_{end}	ending point of the L_4 integration	R_S	radius of a spherical cap
$\mathbf{x}_{\text{start}}$	starting point of the L_4 integration	R'_S	transformed R_S for Case 18 and 19 configurations
η	latitudinal angular parameter for the area integration	S	distance between the infinitesimal surface and a point (x, y, z)
γ	angle between the $+X$ direction and the infinitesimal surface normal vector projected to the XY plane	n/a	not applicable
λ	longitudinal angular parameter for the area integration		
ω	angle between the infinitesimal surface normal direction and the $+Z$ direction		

2. Spherical cap view factor

2.1. Geometrical configurations

In order to discuss view factor solutions, an arbitrary geometrical configuration of a spherical cap and an infinitesimal surface has to be described by certain parameters. Without loss of generality, it can be assumed that the origin of the orthogonal coordinate is at an infinitesimal surface, the center of a spherical cap is on the Z axis, and the top of a spherical cap is on the XZ plane. With these assumptions, a geometrical configuration is described by six parameters as shown in Fig. 1. R_S ($R_S > 0$) is the radius of the spherical cap. d ($d > R_S$) is the distance between the infinitesimal surface and the center of the spherical cap. φ ($0 \leq \varphi \leq \pi$) is the angle between the cap top direction and the $-Z$ direction from the spherical cap center. ω ($0 \leq \omega \leq \pi$) is the angle between the normal direction of the infinitesimal surface and the $+Z$ direction. γ ($-\pi \leq \gamma \leq \pi$) is the angle between the $+X$ direction and the infinitesimal surface normal

The second type L_2 is the line integration along the edge of the spherical cap as shown in Fig. 2 (c). The edge of the spherical cap is described by

$$\begin{bmatrix} x \\ y \\ z \end{bmatrix} = \begin{bmatrix} -R_S \cos \psi \sin \varphi + R_S \cos \alpha \sin \psi \cos \varphi \\ R_S \sin \alpha \sin \psi \\ d - R_S \cos \psi \cos \varphi - R_S \cos \alpha \sin \psi \sin \varphi \end{bmatrix}. \quad (4)$$

The line integration from α_{start} to α_{end} is calculated by

$$\begin{aligned} L_2(\alpha_{\text{start}}, \alpha_{\text{end}}) &= \frac{l_1 A}{4\pi \sin \theta \sin \psi \sin \varphi} \int_{\alpha_{\text{start}}}^{\alpha_{\text{end}}} \frac{l_2 \cos \alpha - l_3}{1 - A \cos \alpha} d\alpha + \frac{m_1 A}{4\pi \sin \theta \sin \psi \sin \varphi} \int_{\alpha_{\text{start}}}^{\alpha_{\text{end}}} \frac{m_2 \sin \alpha}{1 - A \cos \alpha} d\alpha \\ &+ \frac{n_1 A}{4\pi \sin \theta \sin \psi \sin \varphi} \int_{\alpha_{\text{start}}}^{\alpha_{\text{end}}} \frac{n_2 \cos \alpha - n_3}{1 - A \cos \alpha} d\alpha. \end{aligned} \quad (5)$$

The used parameters are defined by Eqs. (6)–(11), and the exact solutions of the integrals in Eq. (5) are shown in Eqs. (12)–(14). It should be noted that the solution is valid in the range of $-\pi < \alpha < \pi$, and the line integration should not cross $\alpha = \pm\pi$.

$$A = \frac{2 \sin \theta \sin \psi \sin \varphi}{1 + \sin^2 \theta - 2 \sin \theta \cos \psi \cos \varphi}, \quad (6)$$

$$l_2 = (1 - \sin \theta \cos \psi \cos \varphi) \sin \theta \sin \psi, \quad (7)$$

$$l_3 = \sin^2 \theta \sin^2 \psi \sin \varphi, \quad (8)$$

$$m_2 = \sin \theta \sin \psi \cos \varphi - \sin^2 \theta \cos \psi \sin \psi, \quad (9)$$

$$n_2 = \sin^2 \theta \cos \psi \sin \psi \sin \varphi, \quad (10)$$

$$n_3 = \sin^2 \theta \sin^2 \psi \cos \varphi. \quad (11)$$

$$\begin{aligned} \int_{\alpha_{\text{start}}}^{\alpha_{\text{end}}} \frac{l_2 \cos \alpha - l_3}{1 - A \cos \alpha} d\alpha &= -\frac{l_2}{A} (\alpha_{\text{end}} - \alpha_{\text{start}}) + \left(\frac{l_2}{A} - l_3 \right) \frac{2}{\sqrt{1 - A^2}} \\ &\times \left\{ \arctan \left(\sqrt{\frac{1 + A}{1 - A}} \tan \frac{\alpha_{\text{end}}}{2} \right) - \arctan \left(\sqrt{\frac{1 + A}{1 - A}} \tan \frac{\alpha_{\text{start}}}{2} \right) \right\}, \end{aligned} \quad (12)$$

$$\int_{\alpha_{\text{start}}}^{\alpha_{\text{end}}} \frac{m_2 \sin \alpha}{1 - A \cos \alpha} d\alpha = \frac{m_2}{A} \{ \log(1 - A \cos \alpha_{\text{end}}) - \log(1 - A \cos \alpha_{\text{start}}) \}, \quad (13)$$

$$\begin{aligned} \int_{\alpha_{\text{start}}}^{\alpha_{\text{end}}} \frac{n_2 \cos \alpha - n_3}{1 - A \cos \alpha} d\alpha &= -\frac{n_2}{A} (\alpha_{\text{end}} - \alpha_{\text{start}}) + \left(\frac{n_2}{A} - n_3 \right) \frac{2}{\sqrt{1 - A^2}} \\ &\times \left\{ \arctan \left(\sqrt{\frac{1 + A}{1 - A}} \tan \frac{\alpha_{\text{end}}}{2} \right) - \arctan \left(\sqrt{\frac{1 + A}{1 - A}} \tan \frac{\alpha_{\text{start}}}{2} \right) \right\}. \end{aligned} \quad (14)$$

The third type L_3 is the line integration on a straight line from the infinitesimal surface to the projection plane. The line from the infinitesimal surface to an arbitrary point (x_a, y_a, z_a) is described by

$$\begin{bmatrix} x \\ y \\ z \end{bmatrix} = s \begin{bmatrix} x_a \\ y_a \\ z_a \end{bmatrix}. \quad (15)$$

Regardless of the range of the parameter s , the integration of Eq. (1) on this line is always zero. Therefore, the L_3 integration result is zero as well.

$$L_3 = 0. \quad (16)$$

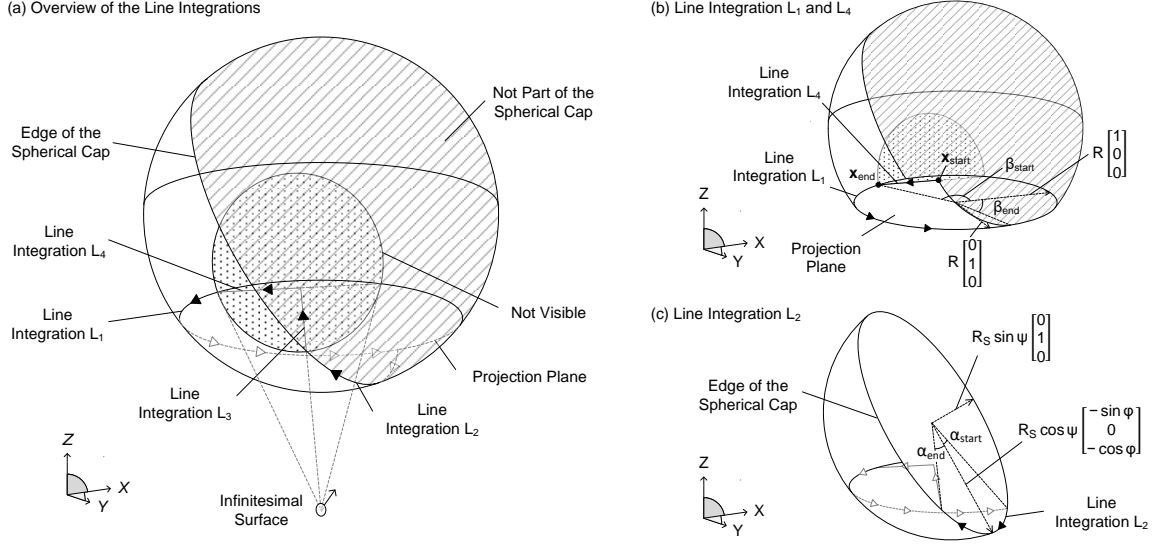


Figure 2: Contour integration consisting of four types of line integrations.

The fourth type L_4 is the integration along a straight line on the projection plane as shown in Fig. 2 (b). The line from $\mathbf{x}_{\text{start}} = (x_{\text{start}}, y_{\text{start}}, h)$ to $\mathbf{x}_{\text{end}} = (x_{\text{end}}, y_{\text{end}}, h)$ is described by

$$\begin{bmatrix} x \\ y \\ z \end{bmatrix} = \begin{bmatrix} x_{\text{start}} + x_{\Delta} t \\ y_{\text{start}} + y_{\Delta} t \\ h \end{bmatrix}, \quad (17)$$

where:

$$x_{\Delta} = x_{\text{end}} - x_{\text{start}}, \quad y_{\Delta} = y_{\text{end}} - y_{\text{start}}, \quad 0 \leq t \leq 1. \quad (18)$$

Based on Eqs.(1) and (17), the result of the line integration is

$$\begin{aligned} L_4(\mathbf{x}_{\text{start}}, \mathbf{x}_{\text{end}}) = & l_1 \frac{hy_{\Delta}}{2\pi \sqrt{AC - B^2}} \left\{ \arctan\left(\frac{A+B}{\sqrt{AC - B^2}}\right) - \arctan\left(\frac{B}{\sqrt{AC - B^2}}\right) \right\} \\ & + m_1 \frac{-hx_{\Delta}}{2\pi \sqrt{AC - B^2}} \left\{ \arctan\left(\frac{A+B}{\sqrt{AC - B^2}}\right) - \arctan\left(\frac{B}{\sqrt{AC - B^2}}\right) \right\} \\ & + n_1 \frac{y_{\text{start}}x_{\Delta} - x_{\text{start}}y_{\Delta}}{2\pi \sqrt{AC - B^2}} \left\{ \arctan\left(\frac{A+B}{\sqrt{AC - B^2}}\right) - \arctan\left(\frac{B}{\sqrt{AC - B^2}}\right) \right\}, \end{aligned} \quad (19)$$

where:

$$A = x_{\Delta}^2 + y_{\Delta}^2, \quad B = x_{\text{start}}x_{\Delta} + y_{\text{start}}y_{\Delta}, \quad C = x_{\text{start}}^2 + y_{\text{start}}^2 + h^2. \quad (20)$$

2.3. Classification and solutions of the spherical cap view factors

The analytical calculation of a spherical cap view factor requires detailed classification. Depending on the geometrical configuration, the view factor calculations are divided into 21 cases. The complete cases and solutions are summarized in Table 1.

The first classification flow chart is shown in Fig. 3, and examples of the geometrical configurations are shown in Fig. 4. In this preliminary classification, five simple configurations are identified (Case 1–5), and the other configurations are divided to two groups. In Case 1, the spherical cap is in the invisible part of the sphere. In Case 2, any part of the sphere is not visible because of the infinitesimal surface direction. Case 3 and Case 4 are practically the same as sphere view factors, since the spherical cap covers the entire area which can be visible from the infinitesimal

Table 1: Spherical cap view factor solutions for each geometrical configuration.

Case	Short description	Classification	Solution
Case 1	Cap Orientation Mismatch	Fig. 3	$F_1 = 0$
Case 2	Infinitesimal Surface Direction Mismatch	Fig. 3	$F_2 = 0$
Case 3	Full Sphere	Fig. 3	Eq. (21)
Case 4	Partial Sphere	Fig. 3	Eq. (22)
Case 5	Full Spherical Cap	Fig. 3	Eq. (28)
Case 6	Partial Cap, No Intersection 1	Figs. 3, 5, 6	$F_6 = 0$
Case 7	Partial Cap, No Intersection 2	Figs. 3, 5, 6	Eq. (35)
Case 8	Partial Cap, No Intersection 3	Figs. 3, 5, 6	Eq. (36)
Case 9	Partial Cap, No Intersection 4	Figs. 3, 5, 6	Eq. (37)
Case 10	Partial Cap, One Intersection 1	Figs. 3, 5, 8	Eq. (38)
Case 11	Partial Cap, One Intersection 2	Figs. 3, 5, 8	Eq. (43)
Case 12	Partial Cap, Two Intersections 1	Figs. 3, 5, 10	Eq. (44)
Case 13	Partial Cap, Two Intersections 2	Figs. 3, 5, 10	Eq. (47)
Case 14	Partial Cap, Two Intersections 3	Figs. 3, 5, 10	Eq. (48)
Case 15	Partial Cap, Two Intersections 4	Figs. 3, 5, 10	Eq. (49)
Case 16	Small Cap, View Direction Mismatch	Figs. 3, 12	$F_{16} = 0$
Case 17	Small Cap, No Intersection	Figs. 3, 12	Eq. (50)
Case 18	Small Cap, No Intersection $\varphi = 0$	Figs. 3, 12	Eq. (51)
Case 19	Small Cap, Two Intersections $\varphi = 0$	Figs. 3, 12	Eq. (52)
Case 20	Small Cap, Two Intersections 1	Figs. 3, 12	Eq. (56)
Case 21	Small Cap, Two Intersections 2	Figs. 3, 12	Eq. (57)

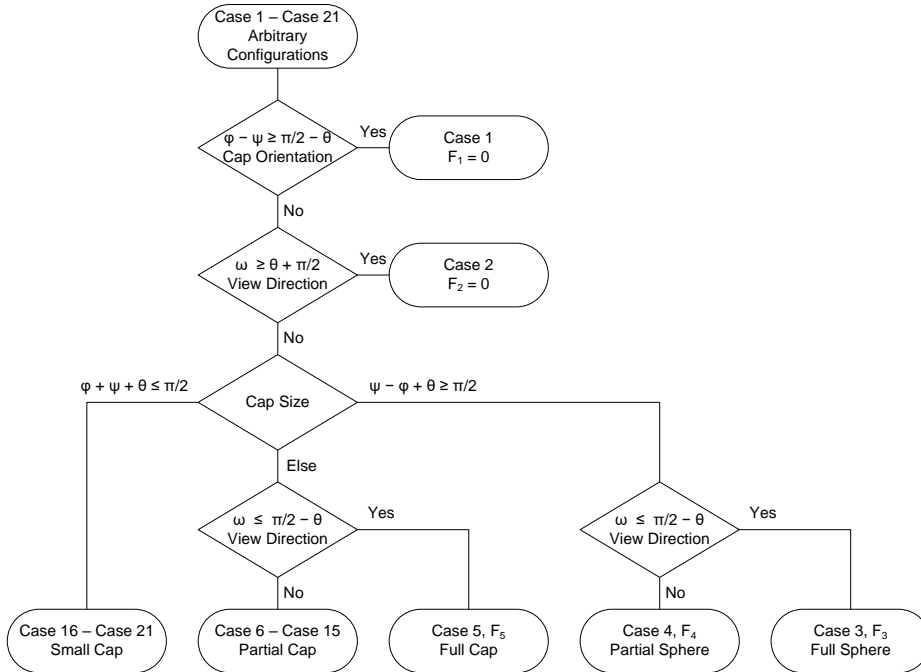


Figure 3: Preliminary classification of arbitrary configurations (Case 1 – Case 21).

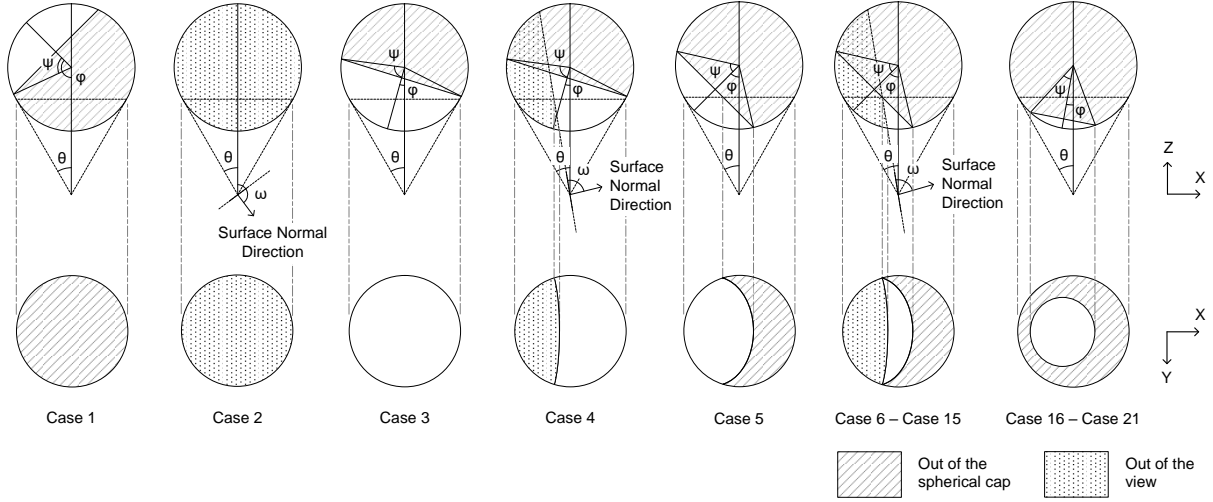


Figure 4: Examples of geometrical configurations for the preliminary classification (Case 1 – Case 21).

surface. A Case 3 view factor is calculated by using the L_1 integration as shown in Eq. (21). This equation means that the given parameters π and $-\pi$ are substituted to β_{start} and β_{end} of Eq. (3).

$$F_3 = L_1(\pi, -\pi). \quad (21)$$

A Case 4 view factor is calculated by a combination of the L_1 and L_4 integration.

$$F_4 = L_1(\gamma + \beta_0, \gamma - \beta_0) + L_4(\mathbf{x}_{\text{start}}, \mathbf{x}_{\text{end}}), \quad (22)$$

where the parameter β_0 is determined by the following relation:

$$R \cos \beta_0 = -h \tan \left(\frac{\pi}{2} - \omega \right), \quad 0 \leq \beta_0 \leq \pi. \quad (23)$$

The starting point $\mathbf{x}_{\text{start}}$ and the ending point \mathbf{x}_{end} of the L_4 integration are

$$\mathbf{x}_{\text{start}} = \begin{bmatrix} R \cos(\gamma - \beta_0) \\ R \sin(\gamma - \beta_0) \\ h \end{bmatrix}, \quad (24)$$

$$\mathbf{x}_{\text{end}} = \begin{bmatrix} R \cos(\gamma + \beta_0) \\ R \sin(\gamma + \beta_0) \\ h \end{bmatrix}. \quad (25)$$

The analytical view factor solutions of Case 3 and Case 4 or the corresponding circular disk view factors are commonly available in the literatures, such as [1–9]. For Case 3, the explicit description of Eq. (21) after the parameter substitution is

$$F_3 = \frac{R^2}{R^2 + h^2} \cos \omega = \frac{R_S^2}{d^2} \cos \omega, \quad (26)$$

which agrees with the solution presented in [1, 2]. Also for Case 4, the explicit description of Eq. (22) can be presented in the following form:

$$F_4 = -\frac{Rh \sin \omega \sin \beta_0}{\pi(R^2 + h^2)} + \frac{R^2 \beta_0 \cos \omega}{\pi(R^2 + h^2)} + \frac{h \sin \omega}{\pi \sqrt{R^2 \cos^2 \beta_0 + h^2}} \arctan \left(\frac{R \sin \beta_0}{\sqrt{R^2 \cos^2 \beta_0 + h^2}} \right) - \frac{R \cos \omega \cos \beta_0}{\pi \sqrt{R^2 \cos^2 \beta_0 + h^2}} \arctan \left(\frac{R \sin \beta_0}{\sqrt{R^2 \cos^2 \beta_0 + h^2}} \right). \quad (27)$$

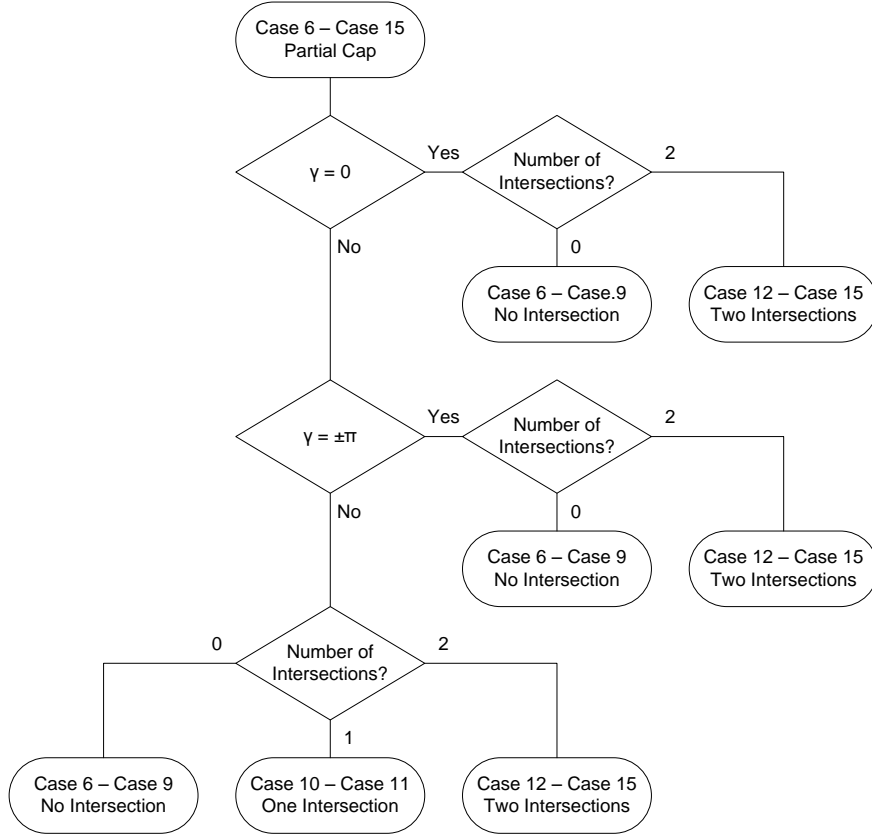


Figure 5: Classification of the partial cap configurations (Case 6 – Case 15).

This equation is further transformed by using Eq. (23) and parameter definitions of h and R . Finally, it is confirmed to be precisely the same as the solution presented in [4, 5]. In Case 5, the contour integration consists of two parts: the edge of the projection plane and the edge of the spherical cap.

$$F_5 = L_1(2\pi - \beta_1, \beta_1) + L_2(\alpha_1, -\alpha_1), \quad (28)$$

where the parameter β_1 and α_1 are determined by the following relations:

$$\cos \beta_1 = -\frac{\cos \psi \sin \varphi}{\cos \theta} + \frac{\sin \theta - \cos \psi \cos \varphi \cos \varphi}{\cos \theta \sin \varphi}, \quad 0 \leq \beta_1 \leq \pi, \quad (29)$$

$$\cos \alpha_1 = \frac{\sin \theta - \cos \psi \cos \varphi}{\sin \psi \sin \varphi}, \quad 0 \leq \alpha_1 \leq \pi. \quad (30)$$

From Case 6 to Case 15, the edge of the spherical cap comes into the visible area. In these cases, the edge of the spherical cap and the edge of the view may have intersections. In this discussion, the interested intersections are those with a Z coordinate of $z \leq h$. Depending on the number of such intersections, they are divided into different cases as shown in Fig. 5. The number of intersections and their coordinates are acquired by solving Eqs. (31)–(33), which correspond to different geometries. Eq. (31) is the sphere surface, Eq. (32) is the plane dividing the spherical cap from the sphere, and Eq. (33) is the edge of the view from the infinitesimal surface. The cases of $\gamma = 0, \pm \pi$ are

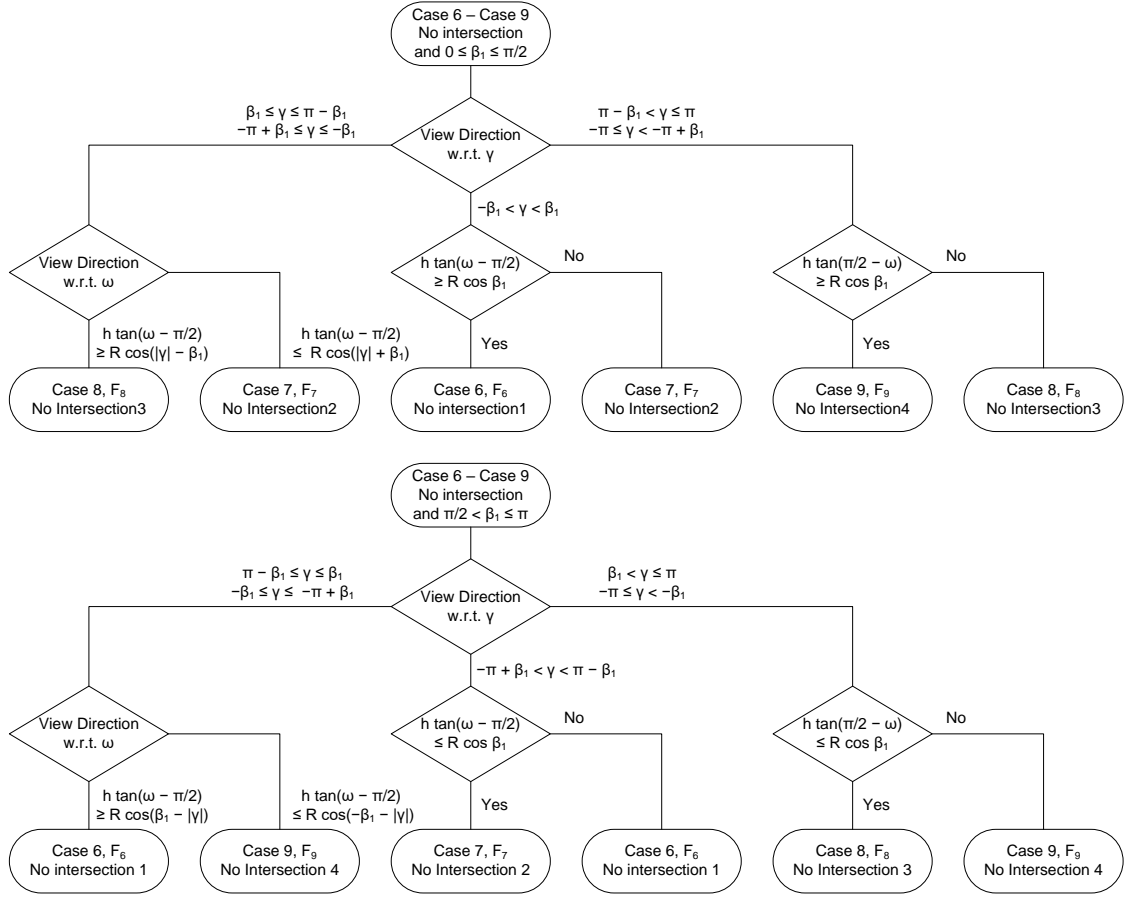


Figure 6: Classification of the no-intersection configurations (Case 6 – Case 9).

handled separately, in order to avoid zero division.

$$x^2 + y^2 + (z - d)^2 = R_S^2, \quad (31)$$

$$(x + R_S \cos \psi \sin \varphi) \sin \varphi + (z - d + R_S \cos \psi \cos \varphi) \cos \varphi = 0, \quad (32)$$

$$x \sin \omega \cos \gamma + y \sin \omega \sin \gamma + z \cos \omega = 0. \quad (33)$$

If there are no intersections between the edge of the spherical cap and the edge of the view, the cases are divided into further four cases. Fig. 6 shows the classification flow chart, and Fig. 7 shows examples of those configurations, viewing from the infinitesimal surface. For each case, a view factor can be calculated by using the already discussed solutions:

$$F_6 = 0, \quad (34)$$

$$F_7 = F_5 + F_4 - F_3, \quad (35)$$

$$F_8 = F_4, \quad (36)$$

$$F_9 = F_5. \quad (37)$$

If there is one intersection, the configurations are divided into two cases. The classification flow chart and configuration examples are shown in Figs. 6 and 9, respectively. A view factor for Case 10 can be calculated as a sum of four line integrations (Fig. 2):

$$F_{10} = L_1(\gamma + \beta_0, \beta_1) + L_2(\alpha_1, \alpha_2) + L_3 + L_4(\mathbf{x}_{\text{start}}, \mathbf{x}_{\text{end}}). \quad (38)$$

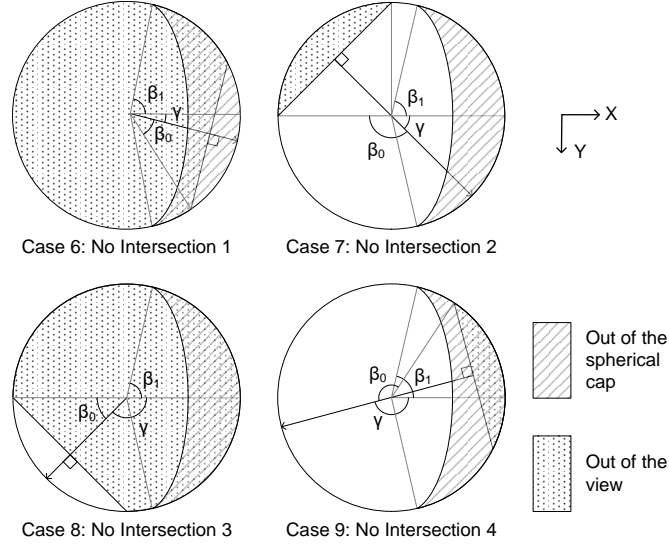


Figure 7: Examples of the no-intersection configurations (Case 6 – Case 9).

Assuming that coordinates of the intersection are $\mathbf{x}_2 = (x_2, y_2, z_2)$, the parameter α_2 can be determined by the following relations:

$$\cos \alpha_2 = \frac{x_2 + R_S \cos \psi \sin \varphi}{R_S \sin \psi \cos \varphi}, \quad (39)$$

$$\sin \alpha_2 = \frac{y_2}{R_S \sin \psi}, \quad (40)$$

where the range of α_2 is $-\pi < \alpha_2 \leq \pi$. The other parameters, β_0 , β_1 and α_1 are determined by Eqs. (23), (29) and (30), respectively. The starting point and the ending point of the L_4 integration are:

$$\mathbf{x}_{\text{start}} = \frac{h}{z_2} \mathbf{x}_2, \quad (41)$$

$$\mathbf{x}_{\text{end}} = \begin{bmatrix} R \cos(\gamma + \beta_0) \\ R \sin(\gamma + \beta_0) \\ h \end{bmatrix}. \quad (42)$$

The order of Case 11 contour integration is different from that of Case 10, but it is possible to find a corresponding Case 10 configuration by rotating the infinitesimal surface direction around the Z axis. Therefore, the solution of Case 11 can be described by using the solution of Case 10 as shown in Eq. (43).

$$F_{11}(d, R_S, \varphi, \omega, \gamma, \psi) = F_{10}(d, R_S, \varphi, \omega, -\gamma, \psi). \quad (43)$$

The cases of two intersections are divided into four cases. The classification flow chart is shown in Fig. 10 and configuration examples are presented in Fig. 11. A view factor of Case 12 is calculated as a sum of four line integrations as shown in Eq. (44). The first L_2 integration is along the edge of the spherical cap, the second L_3 integration is on the line from one intersection to the projection plane, the third L_4 integration is on the projection plane, and the fourth L_3 integration is on the line from the projection plane to the other intersection. As already discussed, two L_3 integrations are zero.

$$F_{12} = L_2(\alpha_2, \alpha_3) + L_3 + L_4(\mathbf{x}_{\text{start}}, \mathbf{x}_{\text{end}}) + L_3. \quad (44)$$

Assuming that the intersections are $\mathbf{x}_2 = (x_2, y_2, z_2)$ and $\mathbf{x}_3 = (x_3, y_3, z_3)$, the corresponding α_2 and α_3 are determined by substituting these parameters to Eqs. (40) and (39). The intersections are acquired by solving Eqs. (31)–(33), and

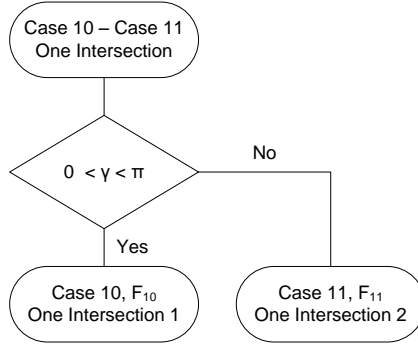


Figure 8: Classification of the one-intersection configurations (Case 10 and Case 11).

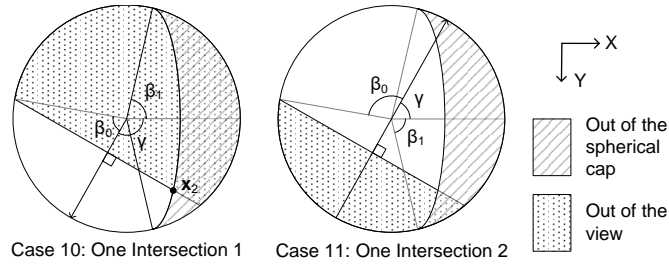


Figure 9: Examples of the one-intersection configurations (Case 10 and Case 11).

the numbering of the intersections has to be selected so that $\alpha_2 > \alpha_3$. With regard to the L_4 integration, the starting point and the ending point are

$$\mathbf{x}_{\text{start}} = \frac{h}{z_3} \mathbf{x}_3, \quad (45)$$

$$\mathbf{x}_{\text{end}} = \frac{h}{z_2} \mathbf{x}_2. \quad (46)$$

The other cases can be calculated by using the result of Case 12:

$$F_{13} = F_5 - F_{12}, \quad (47)$$

$$F_{14} = F_4 - (F_3 - F_5 - F_{12}), \quad (48)$$

$$F_{15} = F_4 - F_{12}. \quad (49)$$

From Case 16 to Case 21, the entire spherical cap is within the possible visible area of the sphere. The classification flow chart and configuration examples are shown in Figs. 12 and 13, respectively. In Case 17, a view factor can be calculated as a complete round of the L_2 integration. Since the parameter range of the L_2 integration is $-\pi < \alpha < \pi$, a round of the L_2 integration is calculated as a limit value.

$$F_{17} = \lim_{\delta \rightarrow +0} L_2(\pi - \delta, -\pi + \delta). \quad (50)$$

Cases of $\varphi = 0$ need to be handled separately as Case 18 and Case 19. In these cases, view factors can be calculated by using the solutions of Case 3 and Case 4, with the parameter transformation.

$$F_{18}(d, R_S, \varphi, \omega, \gamma, \psi) = F_3(d', R'_S, \varphi, \omega, \gamma, \psi), \quad (51)$$

$$F_{19}(d, R_S, \varphi, \omega, \gamma, \psi) = F_4(d', R'_S, \varphi, \omega, \gamma, \psi). \quad (52)$$

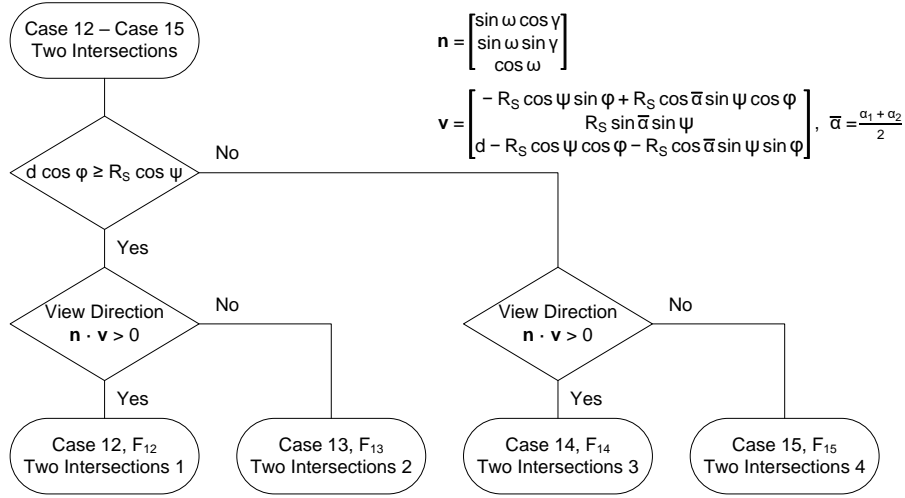


Figure 10: Classification of the two-intersection configurations (Case 12 – Case 15).

The parameter transformation is performed by

$$R'_S = \frac{R_S \sin \psi}{\cos \theta'}, \quad (53)$$

$$d' = d - R_S \cos \psi + R'_S \sin \theta', \quad (54)$$

where:

$$\tan \theta' = \frac{R_S \sin \theta}{d - R_S \cos \psi}. \quad (55)$$

Fig. 14 shows the geometrical meaning of the parameter transformation. The transformation corresponds to replacing the original spherical cap with a new sphere with the same view factor.

The integrations of Case 20 and Case 21 are described by

$$F_{20} = L_2(\alpha_2, \alpha_3) + L_3 + L_4(\mathbf{x}_{\text{start}}, \mathbf{x}_{\text{end}}) + L_3, \quad (56)$$

$$F_{21} = \lim_{\delta \rightarrow +0} L_2(\pi - \delta, -\pi + \delta) + L_2(\alpha_2, \alpha_3) + L_3 + L_4(\mathbf{x}_{\text{start}}, \mathbf{x}_{\text{end}}) + L_3. \quad (57)$$

For both cases, the parameter α_0, α_1 are determined by Eqs. (39) and (40), and the starting point and the ending point of the L_4 integration can be determined by Eqs. (45) and (46). In Case 21, the L_2 integration is described as a sum of two terms, in order to avoid crossing $\alpha = \pm\pi$ during the line integration.

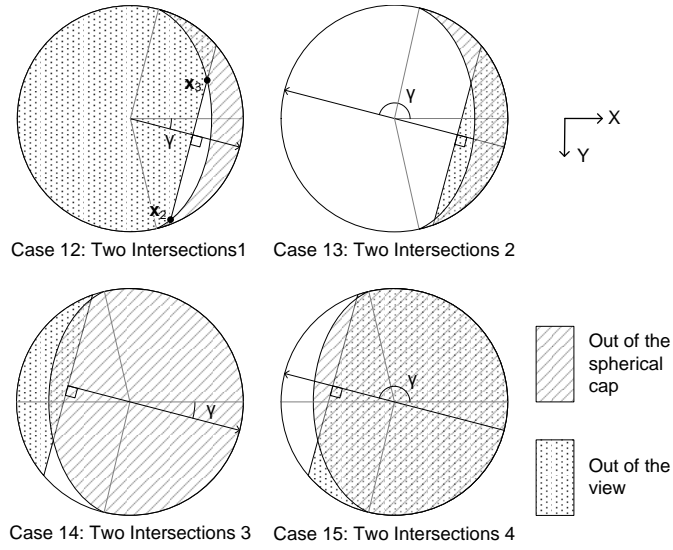


Figure 11: Examples of the two-intersection configurations (Case 12 – Case 15).

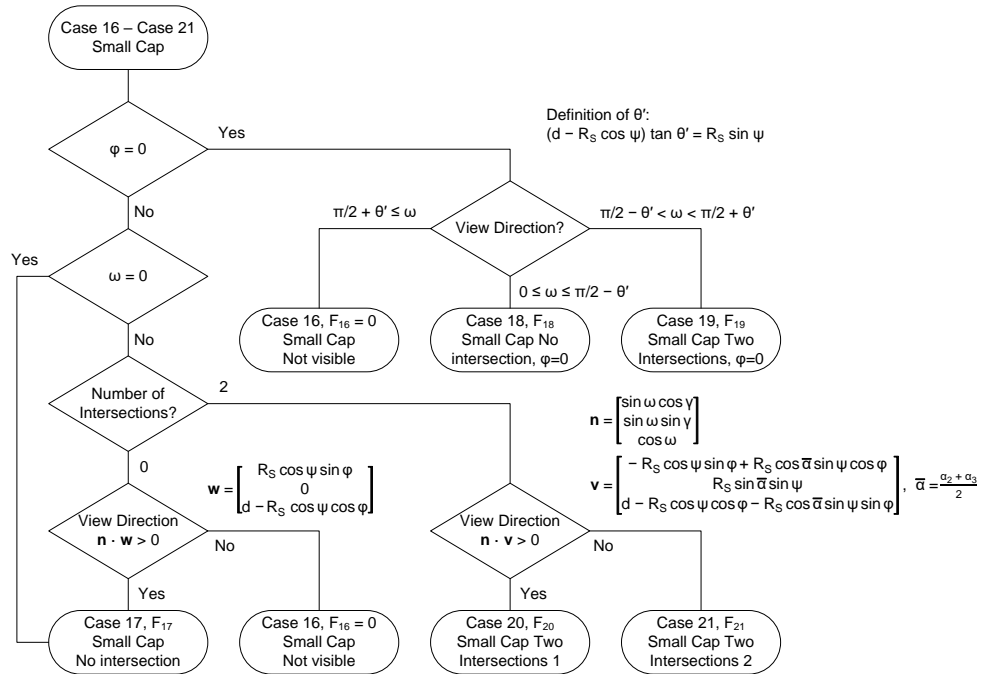


Figure 12: Classification of the small cap configurations (Case 16 – Case 21).

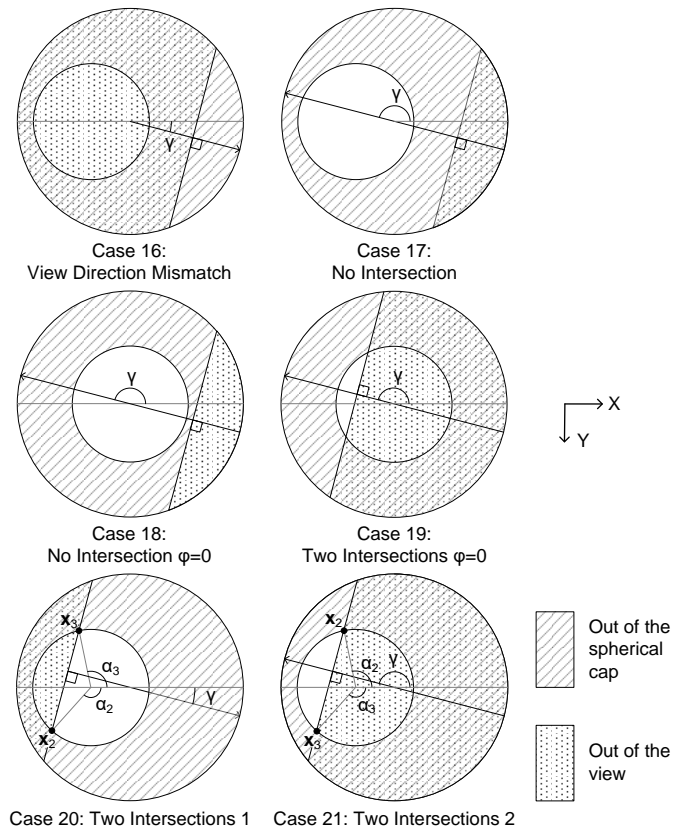


Figure 13: Examples of the small cap configurations (Case 16 – Case 21).

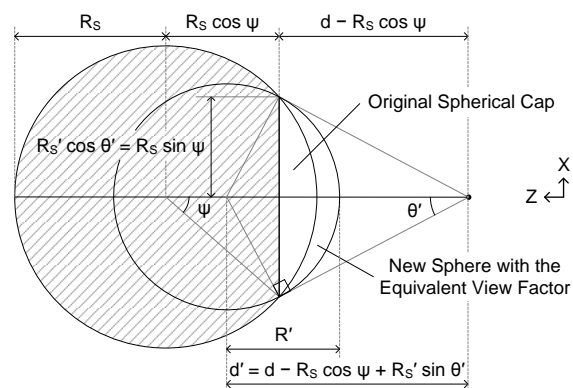


Figure 14: Parameter transformation for the $\varphi = 0$ configurations (Case 18 and Case 19).

2.4. Comparison of view factor calculation results

For an arbitrary geometrical configuration, it is possible to analytically calculate a spherical cap view factor by using the presented classification flow and the solutions. This analysis process is implemented in a Python script and tested for various parameter sets. The calculation results are compared with two different numerical results. The first method is the numerical area integration based on the view factor definition. The integration is performed on the spherical surface described by

$$\begin{bmatrix} x \\ y \\ z \end{bmatrix} = R_S \begin{bmatrix} \sin \eta \cos \lambda \\ \sin \eta \sin \lambda \\ \cos \eta \end{bmatrix} + \begin{bmatrix} 0 \\ 0 \\ d \end{bmatrix}, \quad (58)$$

where η and λ are angular parameters in the latitudinal and longitudinal direction, as shown in Fig. 15. During the numerical area integration, each facet of the spherical surface is determined if it is a part of the spherical cap and visible from the infinitesimal surface by the following conditions:

$$\begin{bmatrix} x \\ y \\ z \end{bmatrix} \cdot \begin{bmatrix} \sin \omega \cos \gamma \\ \sin \omega \sin \gamma \\ \cos \omega \end{bmatrix} > 0, \quad (59)$$

$$\begin{bmatrix} x + R_S \cos \psi \sin \varphi \\ y \\ z - d + R_S \cos \psi \cos \varphi \end{bmatrix} \cdot \begin{bmatrix} -\sin \varphi \\ 0 \\ -\cos \varphi \end{bmatrix} > 0. \quad (60)$$

The integration is described by Eq. (61) based on the view factor definition. For the actual calculation, the longitudinal direction λ is divided into 240 sections, and the latitudinal direction η is divided into 60 sections.

$$F = \int_{\frac{\pi}{2}+\theta}^{\pi} \int_0^{2\pi} \frac{\cos \Theta_0 \cos \Theta_1}{\pi S^2} R_S^2 \sin \eta \, d\lambda d\eta. \quad (61)$$

Θ_0 is an angle between the infinitesimal surface normal and the line connecting the infinitesimal surface and a facet on the spherical surface. Θ_1 is an angle between the normal direction of the facet and the line connecting the infinitesimal surface and the facet. These angles satisfy the following conditions:

$$\cos \Theta_0 = \frac{1}{S} \begin{bmatrix} \sin \omega \cos \gamma \\ \sin \omega \sin \gamma \\ \cos \omega \end{bmatrix} \cdot \begin{bmatrix} x \\ y \\ z \end{bmatrix}, \quad (62)$$

$$\cos \Theta_1 = \frac{1}{SR_S} \begin{bmatrix} x \\ y \\ z - d \end{bmatrix} \cdot \begin{bmatrix} -x \\ -y \\ -z \end{bmatrix}. \quad (63)$$

The second approach is to use the commercial thermal analysis software Thermal Desktop® with the RadCAD® module, which is capable of calculating view factors based on the Monte Carlo ray tracing method [29]. The model consists of two nodes: a circular disk with an area of 1 and a spherical cap surface with a radius of 6.371×10^6 , which correspond to a 1 m² surface and the Earth surface. 1×10^5 rays per node are used to evaluate the view factor.

In Fig. 16, some of the calculation results by the analytical method (Analytical), the numerical area integration (Numerical), and the thermal analysis software (RadCAD) are presented. In the latter two approaches, one general calculation procedure is applied to any configuration. On the other hand, in the analytical approach, one of the 21 cases is determined for each parameter set, and the resulting view factor value is calculated by using the selected solution. The difference between Fig. 16 (a) and (b) is the parameter ψ which defines the spherical cap size. Regarding the cases shown in Fig. 16 (a), the size of the spherical cap ($\psi = 90^\circ$) is larger than the visible area on the spherical surface, which leads to Case 1–15. Meanwhile, many cases shown in Fig. 16 (b) are classified to Case 16–21, because of the smaller cap size ($\psi = 15^\circ$).

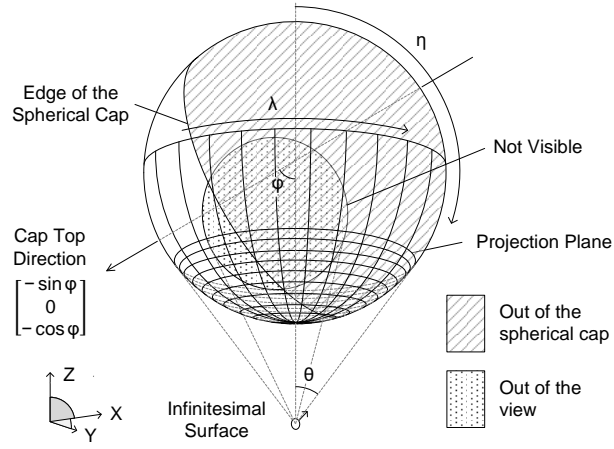


Figure 15: View factor calculation by the numerical area integration.

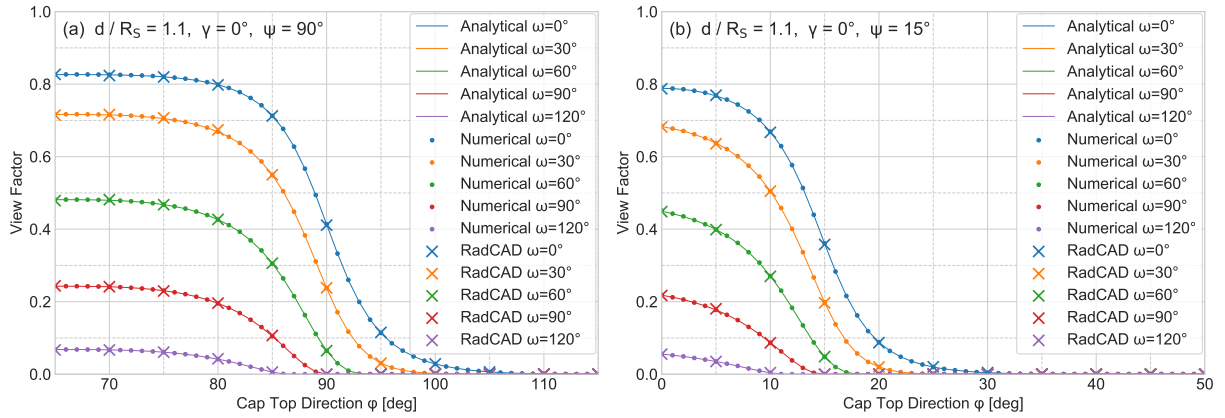


Figure 16: Spherical cap view factors for $d/R_S = 1.1$, $\gamma = 0^\circ$, $\psi = 90^\circ$ and 15° .

Table 2: Tested parameter values on the analytical and numerical methods.

Parameter	Tested values	Number of cases
d/R_S	1.1, 2.0	2
ψ for Numerical	$15^\circ, 30^\circ, \dots, 180^\circ$	12
ψ for RadCAD	$15^\circ, 30^\circ, \dots, 90^\circ$	6
γ for Numerical	$0^\circ, \pm 15^\circ, \dots, \pm 180^\circ$	25
γ for RadCAD	$0^\circ, 30^\circ, \dots, 180^\circ$	7
ω for Numerical	$0^\circ, 15^\circ, \dots, 180^\circ$	13
ω for RadCAD	$0^\circ, 30^\circ, \dots, 180^\circ$	7
φ for Numerical	$0^\circ, 1^\circ, \dots, 180^\circ$	181
φ for RadCAD	$0^\circ, 5^\circ, \dots, 180^\circ$	37

The tested parameter values are summarized in Table 2. The calculations are performed for the entire combinations of these parameter values. The classification result, the calculation time, and the maximum view factor deviation from the Numerical and RadCAD results are summarized in Table 3. The calculation result shows that view factors acquired by the analytical method agree with the results of the numerical methods. The deviations between the analytical and the other results are less than view factor of 0.003 for any Numerical cases, and less than view factor of 0.006 for any RadCAD cases. With regard to the necessary calculation time, the presented values are the average within each case. In general, cases of $90^\circ < \psi < 180^\circ$ requires longer time than cases of $0^\circ < \psi < 90^\circ$. This is because a view factor of $90^\circ < \psi < 180^\circ$ case is calculated by subtracting the corresponding $0^\circ < \psi < 90^\circ$ view factor from the sphere view factor ($\psi = 180^\circ$). Comparing the calculation time for different cases, the most time consuming case is Case 14. As shown in Eq. (48), a view factor of Case 14 is calculated by using view factors of four different cases, which presumably causes longer calculation time than the other cases. Focusing on Case 14 with $90^\circ < \psi < 180^\circ$, the calculation time is compared with the other numerical methods. The exact test case is defined by the following parameters: $d = 1.1$, $R_S = 1.0$, $\psi = 105^\circ$, $\gamma = 180^\circ$, $\omega = 60^\circ$, $\varphi = 100^\circ$. The numerical calculations are performed for different facet size and different number of rays, and the result is summarized in Table 4. For each method, the calculation time is estimated as an average of 100 executions. With regard to RadCAD results, the standard deviation of the 100 executions is presented as well. As shown in the standard deviations in Table 4 and the facet size presented in Fig. 17, it is necessary to increase the number of facets or rays, in order to numerically evaluate a view factor with higher accuracy. For Numerical method, the calculation time linearly increases according to the number of facets. On the other hand, RadCAD calculation time is similar for 1×10^4 , 1×10^5 , and 1×10^6 rays. This indicates that the RadCAD calculation includes a time consuming task which is not part of the ray tracing. Based on the calculation time of 1×10^5 and 1×10^6 rays, it could be estimated that the ray tracing for 1×10^7 rays in this two node model takes approximately 2.1 seconds. For both numerical methods, the number of facets or rays needs to be defined considering on the necessary calculation accuracy and the corresponding calculation cost. On the other hand, by using the analytical method, an analytically exact spherical cap view factor can be acquired with low calculation cost.

Table 3: The number of classified test cases and the averaged calculation time.

Case	Number of cases			Averaged calculation time [μ s]			Maximum view factor deviation	
	15° – 90° *	105° – 180° *	180° *	15° – 90° *	105° – 180° *	180° *	from Numerical	from RadCAD
Case 1	335400	303875	0	7.3	87.1	n/a	0.000432	0.00000
Case 2	107625	83125	27150	54.6	72.3	7.7	0.000000	0.00000
Case 3	15000	7825	31675	117.3	139.4	35.1	0.000432	0.00371
Case 4	44100	26925	58825	238.0	361.0	134.9	0.000374	0.00466
Case 5	80500	63425	0	272.5	258.2	n/a	0.001198	0.00362
Case 6	13836	13888	0	210.6	332.1	n/a	0.000374	0.00000
Case 7	5821	4912	0	505.3	614.4	n/a	0.001222	0.00532
Case 8	7082	4011	0	374.0	471.6	n/a	0.002096	0.00459
Case 9	16030	12049	0	344.9	446.5	n/a	0.001135	0.00336
Case 10	26969	21152	0	523.8	595.5	n/a	0.001123	0.00410
Case 11	26969	21152	0	526.4	593.0	n/a	0.001123	n/a
Case 12	2160	2634	0	489.6	571.4	n/a	0.000983	0.00185
Case 13	2694	2138	0	625.2	684.3	n/a	0.000758	0.00272
Case 14	138	118	0	756.6	831.6	n/a	0.000472	0.00003
Case 15	226	71	0	685.7	679.4	n/a	0.000165	0.00071
Case 16	1077	1162	0	165.5	292.9	n/a	0.000009	0.00000
Case 17	12867	12475	0	204.7	248.3	n/a	0.001208	0.00354
Case 18	450	450	0	173.4	207.6	n/a	0.002319	0.00321
Case 19	400	400	0	265.9	391.9	n/a	0.002027	0.00286
Case 20	3080	3268	0	349.4	479.8	n/a	0.001258	0.00305
Case 21	3476	3195	0	397.3	527.0	n/a	0.001162	0.00283

*The parameter range of ψ .

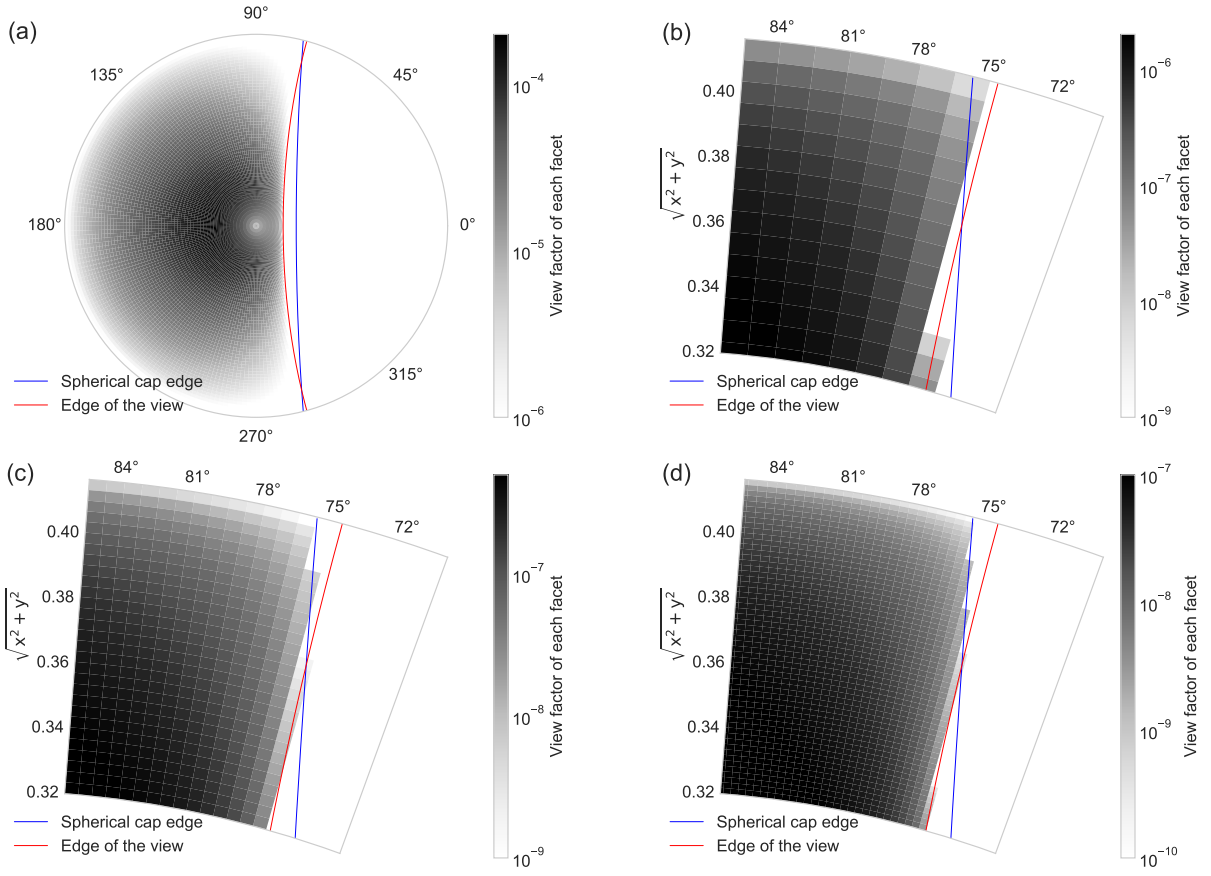


Figure 17: Geometrical configuration of Case 14, $d = 1.1$, $R_S = 1.0$, $\psi = 105^\circ$, $\gamma = 180^\circ$, $\omega = 60^\circ$, $\varphi = 100^\circ$, and the facets for the numerical view factor calculation. (a) for the complete view and (b, c, d) for the section view near the intersection of the spherical cap edge and the view edge. (a, b) 60 sections in the radial direction and 240 sections in the angular direction. (c) 120 sections in the radial direction and 480 sections in the angular direction. (d) 240 sections in the radial direction and 960 sections in the angular direction.

Table 4: Calculation time and accuracy for different view factor calculation methods (Case 14, $d = 1.1$, $R_S = 1.0$, $\psi = 105^\circ$, $\gamma = 180^\circ$, $\omega = 60^\circ$, $\varphi = 100^\circ$).

Calculation method	Calculation time [s]	View factor	Standard deviation
Analytical	0.000834	0.48140759	n/a
Numerical (15×60)*	0.020333	0.4851364	n/a
Numerical (30×120)*	0.067368	0.4822866	n/a
Numerical (60×240)*	0.281720	0.4816237	n/a
Numerical (120×480)*	1.138267	0.4814602	n/a
Numerical (240×960)*	4.427971	0.4814213	n/a
RadCAD (1×10^4 rays)	8.146	0.481426	0.004734
RadCAD (1×10^5 rays)	8.161	0.4812201	0.0014660
RadCAD (1×10^6 rays)	8.338	0.48141795	0.00054163
RadCAD (1×10^7 rays)	10.325	0.48141679	0.00018128
RadCAD (1×10^8 rays)	29.666	0.48143359	0.00004319

*The number of sections for the numerical area integration in the radial and angular direction.

3. Conclusion

The analytical view factor solutions of a spherical cap from an infinitesimal surface are derived. The solutions are classified into 21 cases depending on the geometrical configuration, and the classification procedure is also presented. Actual view factor values are calculated for various parameter sets, and the analytical results agree with the numerical calculation results. By using the analytical solutions, it is possible to evaluate view factors of a spherical cap with reduced calculation cost compared to that of the numerical methods. Therefore, the analytical view factor solutions are useful, especially if a large number of cases need to be evaluated. In addition, spherical cap view factors can be applied not only on the heat transfer evaluation of a spherical cap itself but also on that of a sphere with section-wise different temperatures or different thermal properties.

Acknowledgements

This work was funded by the DLR (German Aerospace Center) research activity Robust Thermal Control System Design. The authors thank Dr. Volodymyr Baturkin for valuable suggestions to improve the manuscript.

References

- [1] J. R. Howell, M. P. Mengüç, Radiative transfer configuration factor catalog: A listing of relations for common geometries, *Journal of Quantitative Spectroscopy and Radiative Transfer* 112 (5) (2011) 910 – 912. doi:10.1016/j.jqsrt.2010.10.002. URL <http://www.sciencedirect.com/science/article/pii/S0022407310003766>
- [2] J. R. Howell, A catalog of radiation heat transfer configuration factors (2010). URL <http://www.thermalradiation.net/>
- [3] F. G. Cunningham, Power input to a small flat plate from a diffusely radiating sphere with application to earth satellites, Tech. Rep. NASA TN D-710 (1961).
- [4] B. T. F. Chung, M. H. N. Naraghi, Some exact solutions for radiation view factors from spheres, *AIAA Journal* 19 (8) (1981) 1077–1081. doi:10.2514/3.7843.
- [5] B. T. F. Chung, M. H. N. Naraghi, A Simpler Formulation for Radiative View Factors From Spheres to a Class of Axisymmetric Bodies, *Journal of Heat Transfer* 104 (1) (1982) 201–204. doi:10.1115/1.3245054.
- [6] M. H. N. Naraghi, B. T. F. Chung, Radiation Configuration Factors Between Disks and a Class of Axisymmetric Bodies, *Journal of Heat Transfer* 104 (3) (1982) 426–431. doi:10.1115/1.3245110.
- [7] M. H. N. Naraghi, Radiation view factors from differential plane sources to disks - a general formulation, *Journal of Thermophysics and Heat Transfer* 2 (3) (1988) 271–274. doi:10.2514/3.96.
- [8] J. M. Cabeza-Lainez, J. A. Pulido-Arcas, M.-V. Castilla, New configuration factor between a circle, a sphere and a differential area at random positions, *Journal of Quantitative Spectroscopy and Radiative Transfer* 129 (2013) 272 – 276. doi:10.1016/j.jqsrt.2013.06.027. URL <http://www.sciencedirect.com/science/article/pii/S0022407313002811>
- [9] J. M. Cabeza-Lainez, J. A. Pulido-Arcas, B. Sanchez-Montañés, C. Rubio-Bellido, New configuration factor between a circle and a point-plane at random positions, *International Journal of Heat and Mass Transfer* 69 (2014) 147 – 150. doi:10.1016/j.ijheatmasstransfer.2013.09.048. URL <http://www.sciencedirect.com/science/article/pii/S0017931013008223>
- [10] R. G. Watts, Radiant Heat Transfer to Earth Satellites, *Journal of Heat Transfer* 87 (3) (1965) 369–373. doi:10.1115/1.3689118.
- [11] M. F. Modest, Solar flux incident on an orbiting surface after reflection from a planet, *AIAA Journal* 18 (6) (1980) 727–730. doi:10.2514/3.7685.
- [12] I. Pérez-Grande, A. Sanz-Andrés, C. Guerra, G. Alonso, Analytical study of the thermal behaviour and stability of a small satellite, *Applied Thermal Engineering* 29 (11) (2009) 2567 – 2573. doi:10.1016/j.applthermaleng.2008.12.038. URL <http://www.sciencedirect.com/science/article/pii/S1359431108005036>
- [13] T. Totani, H. Ogawa, R. Inoue, T. K. Das, M. Wakita, H. Nagata, Thermal design procedure for micro- and nanosatellites pointing to earth, *Journal of Thermophysics and Heat Transfer* 28 (3) (2014) 524–533. doi:10.2514/1.T4306.
- [14] M. Bulut, N. Sozbir, Analytical investigation of a nanosatellite panel surface temperatures for different altitudes and panel combinations, *Applied Thermal Engineering* 75 (2015) 1076 – 1083. doi:10.1016/j.applthermaleng.2014.10.059. URL <http://www.sciencedirect.com/science/article/pii/S1359431114009302>
- [15] A. Farrahi, I. Pérez-Grande, Simplified analysis of the thermal behavior of a spinning satellite flying over sun-synchronous orbits, *Applied Thermal Engineering* 125 (2017) 1146 – 1156. doi:10.1016/j.applthermaleng.2017.07.033. URL <http://www.sciencedirect.com/science/article/pii/S1359431117330685>
- [16] D. P. Mitchao, T. Totani, M. Wakita, H. Nagata, Preliminary thermal design for microsattellites deployed from international space station's kibo module, *Journal of Thermophysics and Heat Transfer* 32 (3) (2018) 789–798. doi:10.2514/1.T5367.
- [17] M. Bonnici, P. Mollicone, M. Fenech, M. A. Azzopardi, Analytical and numerical models for thermal related design of a new pico-satellite, *Applied Thermal Engineering* 159 (2019) 113908. doi:10.1016/j.applthermaleng.2019.113908. URL <http://www.sciencedirect.com/science/article/pii/S1359431118360733>

- [18] J. Li, S. Yan, R. Cai, Thermal analysis of composite solar array subjected to space heat flux, *Aerospace Science and Technology* 27 (1) (2013) 84 – 94. doi:10.1016/j.ast.2012.06.010.
URL <http://www.sciencedirect.com/science/article/pii/S1270963812001083>
- [19] J. Li, S. Yan, Thermally induced vibration of composite solar array with honeycomb panels in low earth orbit, *Applied Thermal Engineering* 71 (1) (2014) 419 – 432. doi:10.1016/j.applthermaleng.2014.07.015.
URL <http://www.sciencedirect.com/science/article/pii/S1359431114005638>
- [20] E. Azadi, S. A. Fazlzadeh, M. Azadi, Thermally induced vibrations of smart solar panel in a low-orbit satellite, *Advances in Space Research* 59 (6) (2017) 1502 – 1513. doi:10.1016/j.asr.2016.12.034.
URL <http://www.sciencedirect.com/science/article/pii/S0273117716307566>
- [21] H. C. HARDEE, D. O. LEE, W. B. BENEDICK, Thermal hazard from lng fireballs, *Combustion Science and Technology* 17 (5-6) (1978) 189–197. doi:10.1080/00102207808946829.
- [22] W. Crocker, D. Napier, Assessment of mathematical models for fire and explosion hazards of liquefied petroleum gases, *Journal of Hazardous Materials* 20 (1988) 109 – 135, major Hazards in the Transport and Storage of Pressure Liquefied Gases. doi:[https://doi.org/10.1016/0304-3894\(88\)87009-2](https://doi.org/10.1016/0304-3894(88)87009-2).
URL <http://www.sciencedirect.com/science/article/pii/0304389488870092>
- [23] Q. xi Zhang, D. Liang, Thermal radiation and impact assessment of the lng bleve fireball, *Procedia Engineering* 52 (2013) 602 – 606, 2012 International Conference on Performance-based Fire and Fire Protection Engineering. doi:10.1016/j.proeng.2013.02.192.
URL <http://www.sciencedirect.com/science/article/pii/S1877705813003111>
- [24] B. K. Dhurandher, R. Kumar, A. Dhiman, Impact assessment of thermal radiation hazard from lpg fireball, *Procedia Earth and Planetary Science* 11 (2015) 499 – 506. doi:10.1016/j.proeps.2015.06.050.
URL <http://www.sciencedirect.com/science/article/pii/S1878522015001010>
- [25] J. Vílchez, M. Muñoz, J. Bonilla, E. Planas, Configuration factors for ground level fireballs with shadowing, *Journal of Loss Prevention in the Process Industries* 51 (2018) 169 – 177. doi:10.1016/j.jlp.2017.12.010.
URL <http://www.sciencedirect.com/science/article/pii/S0950423017306691>
- [26] F. S. Andujar, I. Rodríguez-Cunill, J. M. Cabeza-Lainez, The problem of lighting in underground domes, vaults, and tunnel-like structures of antiquity; an application to the sustainability of prominent asian heritage (india, korea, china), *Sustainability* 11 (20) (2019). doi:10.3390/su11205865.
- [27] M. H. N. Naraghi, Radiative view factors from spherical segments to planar surfaces, *Journal of Thermophysics and Heat Transfer* 2 (4) (1988) 373–375. doi:10.2514/3.56226.
- [28] E. M. Sparrow, A New and Simpler Formulation for Radiative Angle Factors, *Journal of Heat Transfer* 85 (2) (1963) 81–87. doi:10.1115/1.3686058.
- [29] T. D. Panczak, S. G. Ring, M. J. Welch, D. Johnson, B. A. Cullimore, D. P. Bell, *Thermal Desktop® User's Manual, Version 6.1*, C&R Technologies, Inc. (2019).